Ion flux–energy distributions across grounded grids in an RF plasma source with DC-grounded electrodes

OPEN ACCESS
IOP Publishing
Plasma Sources Science and Technology
Plasma Sources Sci. Technol. **31** (2022) 075009 (13pp)
https://doi.org/10.1088/1361-6595/ac7541

Ion flux–energy distributions across grounded grids in an RF plasma source with DC-grounded electrodes

Kunal Soni[1,*], Rodrigo Antunes[1], Roland Steiner[1], Lucas Moser[1,2], Laurent Marot[1] and Ernst Meyer[1]

[1] Department of Physics, University of Basel, Klingelbergstrasse 82, CH-4056, Basel, Switzerland
[2] ITER Organization, Route de Vinon-sur-Verdon, CS 90046, 13067 St Paul Lez Durance Cedex, France

E-mail: kunaldhirajal.soni@unibas.ch

Received 7 February 2022, revised 6 May 2022
Accepted for publication 1 June 2022
Published 10 August 2022

Abstract

We present an experimental investigation of the ion flux–energy distribution functions (IFEDFs) obtained across grounded grids in an asymmetric capacitively coupled RF source using a helium discharge. The powered electrode in the RF source is DC-grounded via a $\lambda/4$ filter, which lifts its DC potential to zero. Grids of different dimensions (hole width, thickness, and geometric transparency) were used to confine the plasma, while the IFEDF of the ion beam departing the grid and reaching the reactor walls was studied using a retarding field energy analyser. The IFEDF obtained was double-peaked, indicating the presence of fast ions arriving from the plasma source, and cold ions generated upon charge exchange collisions between the fast ions and neutrals. The flux, as well as the peak energies of the two ion groups, depended significantly on the process parameters: RF power, He pressure, the distance between grids and walls, and the dimensions of the grids. The results indicate that confining plasma with grids can reduce the ion flux at the walls by over 60%, significantly lowering the wall sputtering rate. This was confirmed with a dedicated long-exposure plasma discharge with a gridded plasma reactor, wherein less than 1 nm of Cu deposition was found on the DC-grounded powered electrode, and the surface reflectivity was preserved to pristine values. In contrast, a similar experiment in a gridless reactor resulted in Cu deposition of 35 nm with a drastic drop in surface reflectivity. These studies are of great importance for the application of similar RF plasma sources with *in-situ* cleaning of diagnostic mirrors in fusion devices, as well as in a variety of plasma processing applications.

Keywords: RF plasma, ion flux, ion beam, ion energy distribution, grids

Supplementary material for this article is available online

(Some figures may appear in colour only in the online journal)

* Author to whom any correspondence should be addressed.

1. Introduction

Capacitively coupled RF (CCRF) sources are one of the most commonly used methods employed to sustain plasma discharge in industry and the laboratory. CCRF plasmas are used in a variety of applications, which make use of the interaction of active species (ions and radicals) created in the plasma volume with the surface materials of the electrodes. As an RF current can flow through dielectric materials, CCRF plasmas can be sustained with dielectric electrode surfaces as well in addition to conducting ones. This significantly broadens their domain of applications. Under-energetic ion bombardment, materials can be selectively removed using such plasma sources (e.g. Si and SiO_2 etching in microelectronics) while at low energies, deposition processes may be utilised (e.g. creation of amorphous Si layers for photovoltaic devices). The microstructure and wettability of surfaces can be modified as well, which is of paramount importance for medical implants [1–4].

The ion flux–energy distribution function (IFEDF) is one of the most important properties in all the above-mentioned applications. As the name suggests, it gives the flux–energy distribution of ions arriving at the surface. In addition to the ion species, the IFEDF primarily defines the processes that occur at the electrode surfaces. The shape of the IFEDF depends on two particular parameters: (i) the collisionality of the sheaths at the electrodes, and (ii) the ratio of the ion transit time τ_i and the RF time period τ_{RF} [5–7]. The collisionality of sheaths depends primarily on the gas pressures. At high pressures, the sheaths are highly collisional, and the majority of the ions undergo several collisions in the sheath before reaching the electrode surface. This lowers their energy, leading to the formation of low-energy peaks in the IFEDF. At low pressures, on the other hand, the sheaths are generally collisionless and the ions have a longer mean free path. In such conditions, they can acquire high energies while traversing the sheath, leading to the presence of predominantly high energy peak(s) in the IFEDF. In the collisionless sheaths, the shape of the IFEDF also depends critically on the ratio of τ_i and τ_{RF}. When $\tau_i/\tau_{RF} \ll 1$, the ions transit the sheath in a fraction of the RF period, making their energy dependent on the instantaneous sheath potential. In this scenario, the IFEDFs are double-peaked, with the maximum and minimum peak energies corresponding to the ions crossing the sheath during the maximum and minimum sheath potential, respectively. On the other hand, when $\tau_i/\tau_{RF} \gg 1$, the ions cross the sheath over multiple RF periods. In this case, the ion energy depends on the time-averaged sheath potential, resulting in a single-peak IFEDF.

The plasma sheath also tends to mold around complex surfaces, a property which finds several applications in plasma processing, such as coating of curved surfaces and plasma immersion ion implantation [8]. Particularly relevant for this article is the plasma sheath interaction with metallic grids. They are used mainly for the extraction of ions from plasma and constitute the fundamental component in the designs of ion and neutral beam sources [9–11], ion thrusters [12], etc. The flux, energy, and directionality of ions extracted from the plasma depend critically on the shape of the plasma–sheath boundary over the grids. The topography of the sheath boundary is determined mainly by the ratio of the sheath thickness L_{sh} and the grid hole width w_g [13]. The different scenarios of plasma–grid interaction are illustrated in figure 1. When $L_{sh}/w_g \gg 1$, as displayed in figure 1(a), the sheath boundary over the grid holes remains nearly planar, identical to that over a solid surface. The ion beam departing from the grids in this case is collimated (assuming the sheath is collisionless). At the other extreme, when $L_{sh}/w_g \ll 1$ (figure 1(b)), the sheath boundary follows the contour of the grid hole boundary. In this particular case, the plasma leaks out of the grid holes and the departing beam is divergent. In the intermediate case where $L_{sh}/w_g \sim 1$ (figure 1(c)), the plasma is largely confined at the grids, but the sheath boundary bends along the grid holes. The degree of sheath bending and the ion beam divergence increase as L_{sh}/w_g decreases. The directionality of the ion beam also depends considerably on the axial thickness of the grid holes (t_g) and in particular on the aspect ratio t_g/w_g [9]. When $t_g/w_g > 1$ (figure 1(d)), the beam divergence decreases as the diverged ions collide with the grid side walls and neutralise. This also increases the neutral formation occurring due to ion collisions with the grounded grid, leading to an increasing neutral flux and a diminishing ion flux in the departing beam. The degree of sheath molding around the grids also influences the effective ion flux transparency of the departing beam. With a planar sheath boundary and a corresponding collimated ion beam (figure 1(a)), the ion flux transparency is identical to the geometric transparency of the grid. However, with a bent boundary (figure 1(c)), the ion flux transparency of the beam increases beyond the geometrical grid transparency, with the diverged ions contributing to the increased flux. The control of all the above-mentioned ion beam properties gives rise to a wide spectrum of plasma-processing applications. For instance, neutral beam sources for anisotropic etching applications particularly require collimated beams [14], while surface cleaning or coating via ion-assisted beam deposition make use of divergent beams [15].

This study is conducted with a major emphasis on RF discharge cleaning of diagnostic mirrors in ITER [16, 17]. Most optical diagnostic systems in ITER will be composed of metallic 'first mirrors' (FMs) with the purpose of directing light from the fusion plasma toward the diagnostic sensors, while simultaneously shielding them from the energetic neutrons. However, being the initial elements in the diagnostic systems, the FMs will also be subject to deposition of the first wall materials, namely beryllium (Be), tungsten (W), and their oxides, causing degradation of their optical properties. They would thus require regular surface conditioning, which is foreseen to be achieved via an *in-situ* CCRF discharge cleaning system [17]. This system employs FMs as the powered electrodes to generate CCRF discharges, wherein they develop a negative self-bias and undergo ion sputtering [18–21]. However,

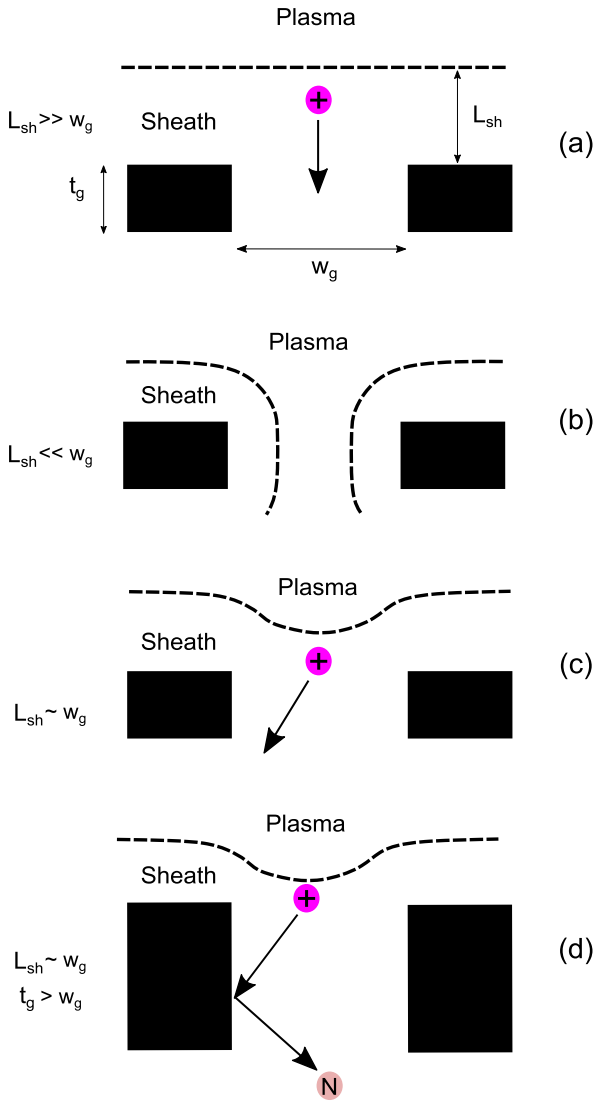

Figure 1. A schematic representation of plasma molding around grid holes with different dimensions of sheath thickness L_{sh}, grid hole width w_g and axial grid hole thickness t_g: (a) when $L_{sh} \gg w_g$ with a planar sheath boundary (represented by the dashed line), (b) when $L_{sh} \ll w_g$ with leaked plasma, (c) when $L_{sh} \sim w_g$ with a bent boundary and (d) when $L_{sh} \sim w_g$ and $t_g > w_g$, leading to grid-induced ion neutralisations.

in ITER the FMs will also be actively water-cooled to tackle the high thermal loads deposited on the mirrors via gamma and neutron radiation. The physical contact of the grounded water cooling lines with the FMs leads to their RF grounding, disabling the excitation of CCRF discharges. To overcome this challenge, the water-cooling lines are foreseen to be implemented as a quarter-wavelength ($\lambda/4$) filter, commonly referred to as the notch filter [22, 23]. The presence of a $\lambda/4$ filter DC-grounds the FMs, but allows RF propagation to generate RF discharges [24]. On the short end, however, adding a $\lambda/4$ filter increases the plasma potential to several hundred volts (in contrast to a few tens of volts typically observed in highly asymmetric CCRF plasma) [24–29]. A high plasma potential considerably increases the erosion of the wall surfaces surrounding FMs, which in turn get re-deposited on FMs, thus making the plasma cleaning process ineffective. This was discussed in detail in our previous study [30]. To achieve the goal of cleaning DC-grounded mirrors, it is hence necessary to investigate strategies that minimise the wall sputtering and their consequent deposition on mirrors. We address that topic in this manuscript, using the property of plasma confinement via grounded grids. The results can also be extended to applications that aim to minimise ion-assisted wall erosion that reduces the lifetime of plasma reactors, such as ion thrusters [12].

In this study we investigate the plasma–grid interactions and their influence on the IFEDFs obtained at the walls of a CCRF plasma reactor with DC-grounded electrodes. Within this investigation, we study the IFEDFs with varying system geometry and plasma parameters. Building on that, we also investigate the impact of grids on the reactor wall sputtering and consequent re-deposition on the powered electrodes. The CCRF plasma reactor mimics a first mirror unit with ITER-relevant geometry, hence the results are directly relevant within the scope of a mitigation strategy for FM cleaning with a $\lambda/4$ filter.

2. Experimental

2.1. Experimental setup

The experiments were performed in a plasma reactor placed inside a high-vacuum chamber at the University of Basel (figure 1 in [31]). A schematic of the experimental setup is presented in figure 2. The unit has square cuboid geometry (250 mm × 150 mm × 200 mm) and holds two unpolished molybdenum (Mo) electrodes (100 mm × 100 mm × 9 mm), M1 and M2, placed in grounded holders on the opposite walls. M1 was used as the powered electrode, while M2 was kept either electrically grounded or floating. The body of the unit was made of copper and served as the grounded electrode. A 60 MHz RF generator (cito-plus COMET) coupled with a matchbox was used to generate a helium plasma inside the unit.

Both M1 and M2 hold three circular Mo insets ($\oslash = 26$ mm), which could be detached from the mirror for characterization. The top surface of the insets was polished with silicon carbide paper, diamond paste and 0.05 μm alumina powder to obtain a highly reflective surface. The insets were electrically connected to M1 and M2, implying they served as a part of the electrodes.

Three different stainless steel grids were used in the experiments, the dimensions of which are presented in table 1. They were inserted in the unit between M1/M2 and the bottom wall, as observed in figure 2, and electrically connected to the walls to ensure they were grounded. They could be moved vertically in the unit, such that the distance between the grid and the bottom wall could be varied. As the measurements are carried out using a retarding field energy analyser (RFEA), the distance of the grid is measured from the top of the RFEA sensor and is referred to as d_g in this manuscript (figure 2). An image of the reactor with the grids and RFEA can be observed in figure S1 (https://stacks.iop.org/PSST/31/075009/mmedia) in the supplementary information.

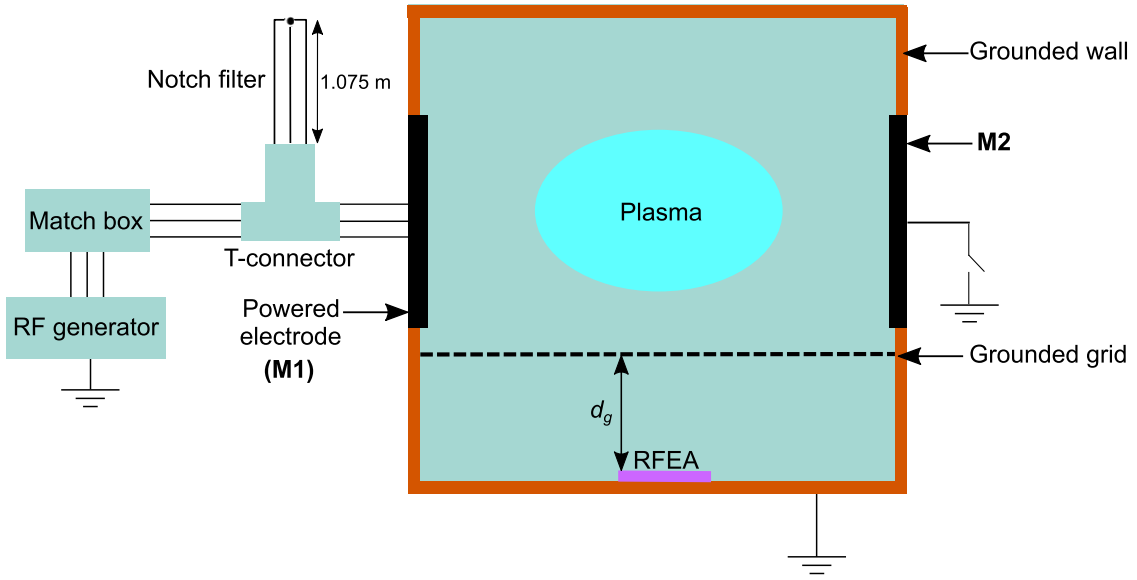

Figure 2. A schematic representation of the experimental setup. The plasma is generated inside the reactor using a 60 MHz generator with a matchbox and the notch filter is connected to M1 via a coaxial T-connector. Meanwhile, M2 is floating or grounded, depending on the experiment. The IFEDF of ions passing through the grid is measured by the RFEA, shown in violet.

Table 1. Dimensions of the grids used in the experiments.

Grid	Hole width (w_g) (mm)	Wire thickness (t_g) (mm)	Transparency (%)
G1	1.60	0.22	77.0
G2	3.15	0.56	72.0
G3	5.00	1.00	69.4

Table 2. The electrode characteristics and discharge parameters in the experiments.

Experimental parameters	Value
Powered area (M1) A_p	100 cm^2
Grounded area A_g	2440 cm^2
Notch filter length	1.075 m
Driving frequency	60 MHz
RF power	120 W
He pressure	1 Pa

In the reference configuration (without grids), the geometrical area A_p of the powered electrode (M1) is 100 cm^2, while that of the grounded body, A_g, is 2440 cm^2. Accordingly, the geometrical ratio of the grounded to the powered surfaces was $A_g/A_p = 24.4$, which makes the discharge highly asymmetric. It is important to note that the effective area ratio, determined by the grounded area in contact with the RF plasma, can be different from the geometrical area ratio, depending on the discharge parameters. The area asymmetry of the system ideally results in the development of a negative self-bias at M1. The DC bias, however, is short-circuited by the addition of a notch filter at the powered electrode. The notch filter was achieved using an RF transmission line with a physical length of 1.075 m with a short-circuit at one of its ends, while the other end was connected to the system via a T-connector (figure 2). The details of the notch filter are presented in our previous publications [24, 30]. Consequently, a CCRF discharge is excited while DC-grounding the powered electrode at the same time. The discharge parameters are presented in table 2.

2.2. Characterization techniques

The IFEDF of the ions reaching the wall of the plasma reactor was measured using a Semion^{TM} single sensor RFEA (Impedans, Ltd) [32, 33]. The measurements were analyzed using the Semion System^{TM} software to obtain the IFEDF, including the ion current density (J_i) and the mean ion energy ($\bar{E}_i$). The typical uncertainties for the measurements in J_i and E_{ion}, as provided by Impedans, Ltd, are $\pm 20\%$ and $\pm 2\%$ (in addition to ± 1 eV resolution), respectively.

The surface chemical composition of the insets on M1 and M2 was obtained using x-ray photoelectron spectroscopy (XPS). The electron spectrometer is equipped with a hemispherical analyzer (Leybold EA10/100 MCD), and a non-monochromatized Mg Kα x-ray source ($h\nu = 1253.6$ eV) was used for core-level spectroscopy. The binding energy scale was calibrated using the Au $4f_{7/2}$ line of a cleaned gold sample at 84.0 eV. The fitting procedure of the core-level line is described in a previous publication [34]. Additionally, where necessary, the insets were characterised using energy-dispersive x-ray (EDX) spectroscopy. The thickness of surface layers was obtained by fitting the EDX data using STRATAGem software [35–37], the procedure of which is described elsewhere [38]. The EDX measurements were performed using the SEM-FEI Nova Nano SEM23 microscope, varying the acceleration voltage from 3 to 20 kV. The UV–Vis–NIR total and diffuse reflectivity (250–800 nm) of the insets were recorded using a Varian Cary 5 spectrophotometer. The specular reflectivity could be calculated by subtracting the diffuse component from the total reflectivity.

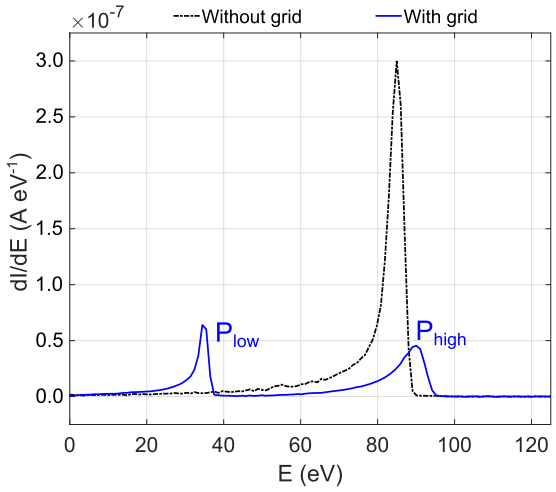

Figure 3. The IFEDF obtained at the wall of the plasma reactor with and without grids, using 120 W/1 Pa He plasma.

3. Results and discussion

3.1. Ion flux–energy distributions across grids—parametric study

The IFEDF of the reference discharge (i.e. without grids) measured at the reactor wall displayed a single sharp peak at 85 eV with a J_i of 1.5 A m^{-2}, as observed in figure 3. The approximate sheath thickness (L_{sh}) can be calculated using the Child–Langmuir law [39, 40],

$$L_{sh} = \frac{2}{3}\left(\frac{2e}{m_i}\right)^{\frac{1}{4}}\left(\frac{\epsilon_0}{J_i}\right)^{\frac{1}{2}}\bar{V}_s^{\frac{3}{4}}, \tag{1}$$

where e is the electronic charge, m_i is the ion mass, ϵ_0 is the vacuum permittivity and $\bar{V}_s$ is the time-averaged sheath potential, which roughly corresponds to the peak ion energy (E_i) in the measured IFEDF (i.e. $\bar{V}_s = 85$ V). Hence, using equation (1), we obtain an L_{sh} of 3.8 mm. The sheath can be further examined by looking at the ratio of the ion transit time across the sheath τ_i and the RF time period τ_{RF}, which is given as

$$\frac{\tau_i}{\tau_{RF}} = 3L_{sh}\nu\left(\frac{m_i}{2e\bar{V}_s}\right)^{\frac{1}{2}}, \tag{2}$$

where ν is the excitation (RF) frequency. Using the above equation, we obtain $\tau_i/\tau_{RF} \sim 11$. This implies that the ions cross the sheath in about 11 RF periods; hence, the ion energy depends on the time-averaged rather than the instantaneous sheath potential. This indicates an absence of modulation in the ion energy, resulting in a singly peaked IFEDF as observed.

Following this, grid G2 was placed at $d_g = 35$ mm from the bottom wall (figure 2), and a plasma was generated with the same parameters. As the L_{sh} was identical to the G2 hole width ($w_g = 3.15$ mm), the plasma was confined in the reactor above the grid. An image of the confined plasma above the grid in the experiment can be observed in figure S2 of the supplementary information. It is worth noting that some plasma still exists in the region between the grid and the RFEA, i.e. the plasma penetrates the grid, even with the comparable size of the grid window and the sheath. However, its density drops significantly beyond the grid, leading to its effective confinement. The sheath molding is in the regime of figure 1(c), and the departing ion beam is expected to have a low divergence. Further, the ratio $t_g/w_g \sim 0.2$, indicating minimal grid-induced ion neutralisations. The IFEDF measured at the wall in this case showcased two peaks at roughly 90 eV and 32 eV, respectively (figure 3). These two peaks obtained in the high and low energy intervals within the IFEDF are referred to as P_{high} and P_{low}, respectively. Furthermore, the total J_i of the obtained distribution was significantly lowered to 0.6 A m^{-2}. Moreover, P_{low} was rather discrete, while P_{high} had a higher dispersion. The bulk plasma was characterized with a Langmuir probe, which indicated a plasma potential of roughly 90 V. Hence, P_{high} obtained in the IFEDF corresponds to the fast ions generated in bulk plasma, which accelerate across the sheath at the grid. As the plasma parameters and the geometry were identical to the case without any grid, the sheath properties at the grid are not expected to vary when compared to the previous case. Hence, with $\tau_i/\tau_{RF} \sim 11$, the two-peaked IFEDF cannot be a result of the sheath modulation. This points toward the fact that the cold ions, contributing to the origin of P_{low}, are generated downstream between the grid and the RFEA. These may be created as a result of charge exchange (CX) collisions between the He^+ ions and background He neutrals in the region between the grid and the wall. This can be understood as per the following equation,

$$He^+(1) + He(2) \rightarrow He(1) + He^+(2). \tag{3}$$

Here, $He^+(1)$ are the fast ions that are generated in the plasma source. Upon exiting the grid, they can undergo CX collisions with the background neutrals He(2), which generate cold ions $He^+(2)$ with a lower energy, while the fast ion is neutralised to He(1). The generation of cold ions in an ion beam via resonant CX collisions with background neutrals has been observed before [41, 42]. For a detailed look at the phenomenon, the process parameters were varied to study their impact on the two-peak distribution.

3.1.1. He pressure variation. The He pressure was varied in the range of 0.5 to 3 Pa, keeping all the other parameters the same (table 2). Initially, the IFEDFs were measured at the wall without grids to obtain the sheath characteristics at different pressures. The $\bar{V}_s$ varied between 85 and 90 V in this pressure range, and using equation (1), the L_{sh} was obtained between 3.5 and 4.5 mm. Consequently, the $L_{sh}/w_g \sim 1$ and the plasma–grid interaction remains similar to the varying pressure. Upon installing the grid G2 at $d_g = 35$ mm, the two-peak distribution was visible across the pressure range, and the IFEDF characteristics (ion flux, energy, and dispersion) varied considerably, as observed in figure 4. As the plasma–grid interaction is uniform, the ion directionality, neutralisations, and flux transparency remain unchanged, indicating that variations in the IFEDF arise primarily from processes occurring in the grounded volume between the grid and RFEA.

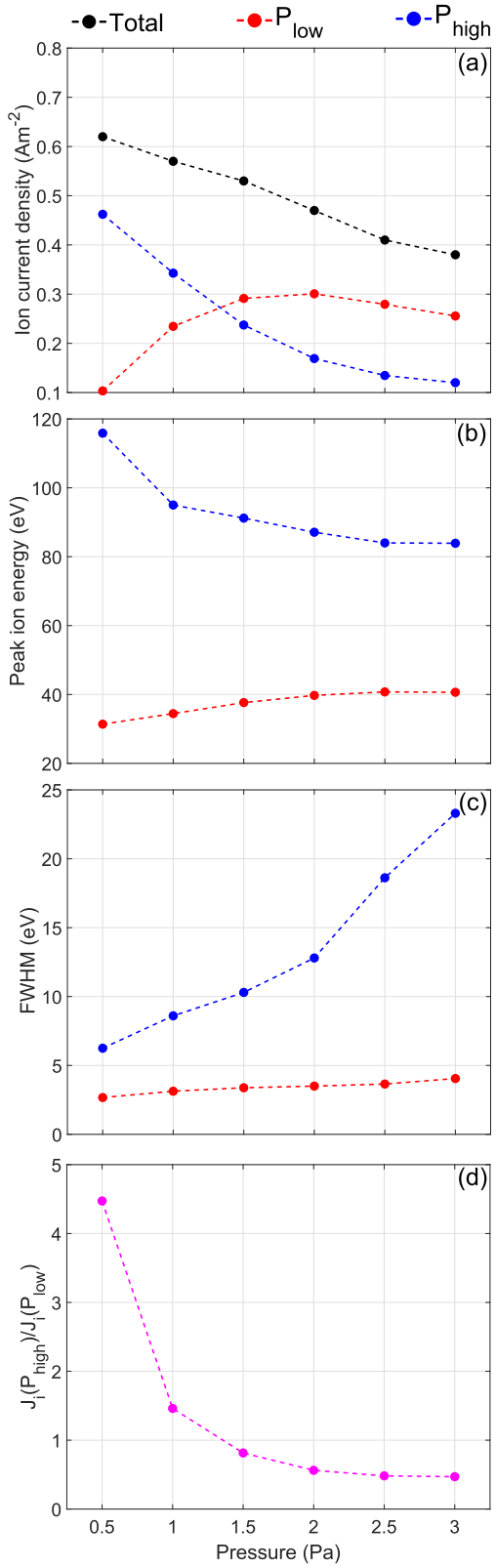

Figure 4. The characteristics of P_{high} and P_{low} extracted from the IFEDF with varying He pressure: (a) ion current densities, (b) peak ion energies, (c) full width half maximums and (d) the ratio of ion fluxes $J_i(P_{high})/J_i(P_{low})$. Constant parameters: 120 W RF power, grid G2 at $d_g = 35$ mm.

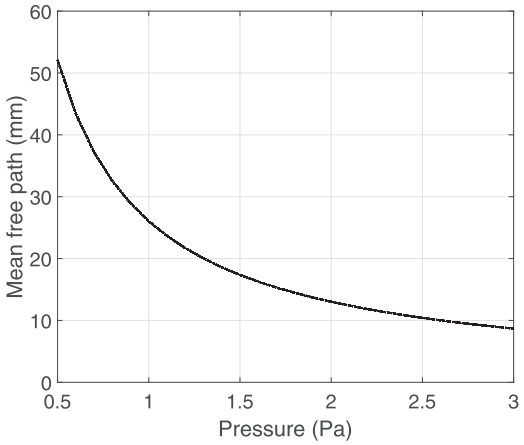

Figure 5. The CX mean free path of He atoms as a function of pressure, obtained from equation (4).

The total J_i was observed to decrease with increasing pressure, as observed in figure 4(a). The individual flux contributions of P_{high} and P_{low} in the IFEDF were obtained by calculating the area under the respective peaks. As displayed in figure 4(a), the flux of P_{high}, and hence fast ions, decreased with the increasing pressure. Simultaneously, the flux of P_{low}, and hence cold ions, increased. The $J_i(P_{low})$ reached a maximum of 0.3 A m^{-2} at 1.5 Pa and decreased for larger pressures as a result of the decrease in the overall flux. This indicates that at low pressure the ion beam is mainly composed of fast ions originating from the plasma source, and increasing the neutral pressure suppresses their population and simultaneously enhances the cold ion density via CX collisions. The peak energy of P_{high}, corresponding to fast ions, also decreased from 115 to 85 eV (figure 4(b)). It is important to note that even though RF power is a constant, changing the pressure results in an arbitrary change in the RF potential amplitude at the electrode. This has a direct impact on the $\bar{V}_s$, and hence the peak energy of P_{high}. However, we cannot comment on it quantitatively due to the lack of experimental data on RF potential amplitudes at the electrode. Simultaneously, the dispersion of P_{high} (quantified via its full width half maximum) increased from 6 to 24 eV, as observed in figure 4(c). This indicates that increasing pressure causes frictional damping of the fast ion beam energy, which lowers its peak energy as well as increases its dispersion. Similar observations were also made in [42]. On the other hand, the peak ion energy of P_{low} increased slightly from 30 to 40 eV, while its dispersion remained roughly a constant.

The attenuation of a fast ion population with pressure can be conveniently examined by studying the ratio of fast vs slow ion flux. As indicated in figure 4(d), the flux ratio ($J_i(P_{high})/J_i(P_{low})$) attenuated with increasing pressure. An identical trend was also reported in [41]. This can be understood by considering the collision dynamics between the fast He^+ ions departing the grids and the background He neutrals. The mean free path (λ) for a certain CX collision is

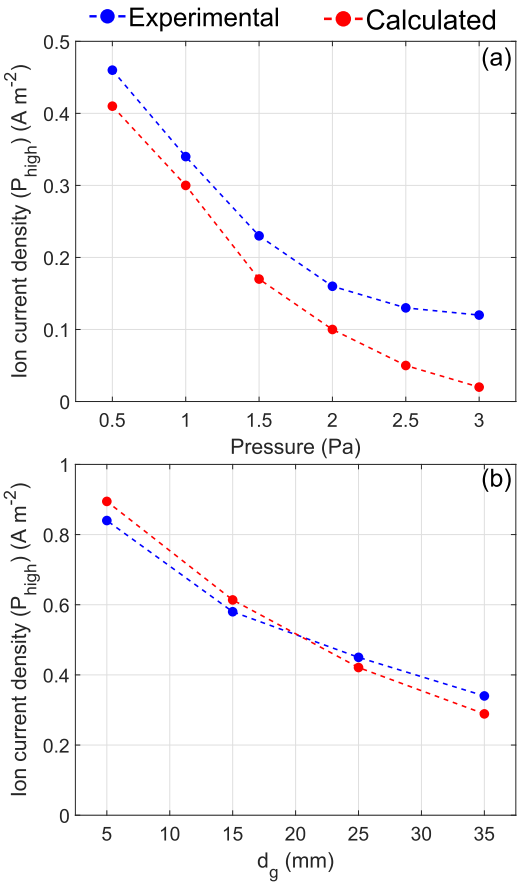

Figure 6. Comparison of the measured fast ion flux and that calculated via equation (5) upon variation of (a) pressure and (b) the distance d_g between grid G2 and RFEA.

given by

$$\lambda = \frac{k_B T}{p\sigma_{CX}}, \tag{4}$$

where k_B is the Boltzmann constant, T is the temperature, p is the pressure and σ_{CX} is the CX collision cross-section. Here, σ_{CX} depends considerably on the incident energy of the colliding species [43]. For He^+–He CX collisions at 90 eV incident energy, the $\sigma_{CX} \sim 1.56 \times 10^{-19}$ m^2 [44]. Using $T = 300$ K, the λ is calculated via equation (2) for the experimental pressure range, and is displayed in figure 5.

As indicated, the λ is roughly 50 mm at $p = 0.5$ Pa, which is in a similar range as d_g (35 mm). This implies a very weak interaction of the fast ion beam with the background neutrals, where they suffer on average $\lesssim 1$ CX collision before reaching the RFEA. This explains the relatively high flux of fast ions obtained at low pressures. Conversely, at the high-pressure end at $p = 3$ Pa, the λ is as low as 8 mm, indicating a much larger probability of interaction between fast He^+ and He neutrals. Hence, increasing the pressure increases the resonant ion–neutral CX collisions, which results in an increased generation of cold ions. Consequently, the total flux is redistributed, wherein the flux of fast ions is transferred to that of cold ions.

The decay in the fast ion flux upon undergoing CX collisions with neutrals can also be calculated using the equation [45, 46],

$$J_{fast}(z) = J_{fast,\,0}\ \exp\left(-\frac{d_g p\sigma_{CX}}{k_B T}\right). \tag{5}$$

Here, $J_{fast}(z)$ is the flux of fast ions obtained after traversing a length of $z = d_g$ in a neutral gas pressure p, while $J_{fast,0}$ is the fast ion flux entering the neutral gas chamber, i.e. at $z = 0$ m. $J_{fast,0}$, in our case, can be roughly taken as the product of J_i without grids and the geometric transparency of G2 (72%). The J_i without grids was measured, wherein it lay between 1.1 and 1.8 A m^{-2} in the pressure range of 0.5 and 3 Pa, respectively. These values were multiplied with the transparency of G2 to obtain $J_{fast,0}$, i.e. $J_{fast,0} = J_i$(without grids) $\times$ 0.72. Then, using $T = 300$ K and $d_g = 35$ mm, $J_{fast}(z)$ was calculated via equation (5) and compared with the measured fast ion flux $J_i(P_{high})$ (with grids) measured via the IFEDF in the pressure range. As observed in figure 6(a), the calculated and measured fast ion flux are in good agreement. This clearly indicates that the fast ion flux indeed attenuates exponentially with increasing pressure due to an increased density of neutrals and corresponding CX collisions.

3.1.2. Grid-RFEA distance (d_g) variation. The IFEDFs were further studied by changing the vertical position of the grid G2 in the setup, varying d_g from 5 to 35 mm in the process. As the RF power and the He pressure are constant here, the sheath properties and consequently the plasma–grid interaction remain unchanged (i.e. $\bar{V}_s = 85$ eV and $L_{sh} = 3.8$ mm). The obtained IFEDF characteristics are displayed in figure 7.

The total J_i decreased with increasing d_g, as observed in figure 7(a). With the increasing d_g, the cold ion flux increased and the fast ion flux decreased, in a fashion similar to that observed in the pressure variation (figure 4(a)). The flux ratio $J_i(P_{high})/J_i(P_{low})$ also diminished with increasing d_g, as observed in figure 7(d), which is again identical to the flux ratio scaling with pressure (figure 4(d)). This attenuation of the fast ion flux can also be explained based on the resonant CX collisions that they undergo through the neutral region, which increases with the length d_g. As $p = 1$ Pa, the λ remains constant at roughly 25 mm. At the lowest point $d_g = 5$ mm there are almost no CX collisions that can occur between the fast ions and the background neutrals, and hence the measured ion flux is composed almost entirely of fast ions. As d_g increases, the CX collision probability increases as well, leading to a rise in the cold ion population. Consequently, the fast ion flux reduces. The decay in the fast ion flux was calculated via equation (5), and was in excellent agreement with the measured values, as indicated in figure 6(b). This indicates that the fast ion flux indeed decays exponentially with increasing d_g upon CX collisions in a neutral volume.

The peak energy of the P_{high} remained constant at roughly 85 eV with varying d_g, as displayed in figure 7(b). As the RF power and He pressure remain constant, the ionization degree as well as the $\bar{V}_s$ at the grid remain the same, explaining the constant energy of the fast ions. Furthermore, the dispersion of P_{high} increases by only 3 eV, indicating that there is no considerable damping of the fast ion energy in this range of d_g.

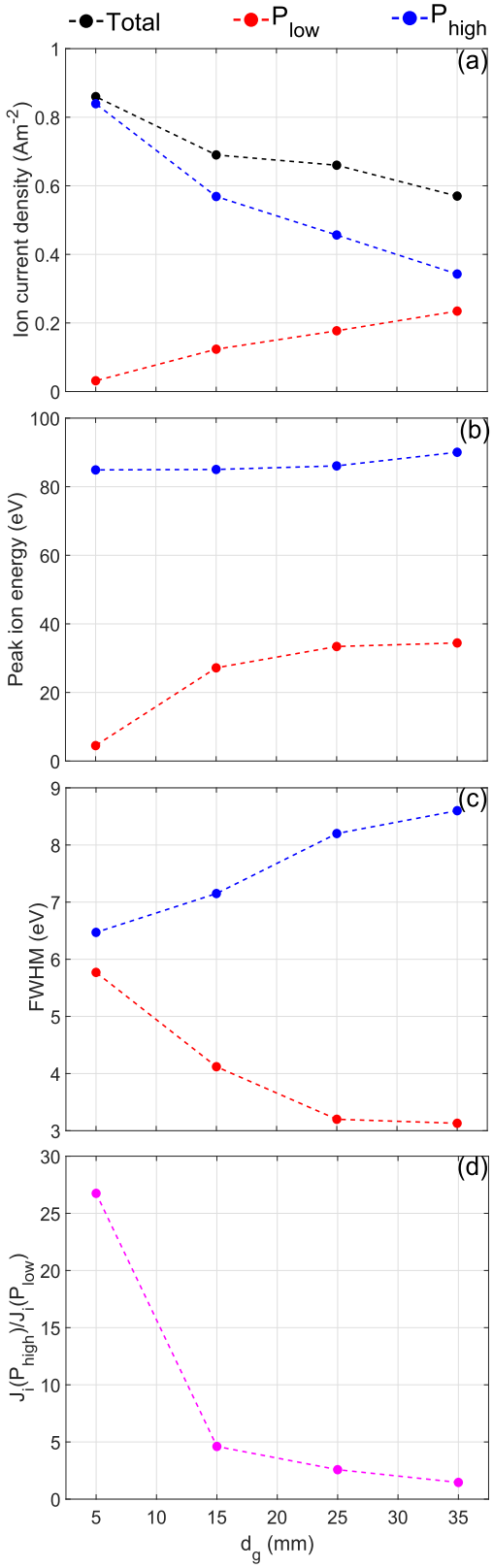

Figure 7. The characteristics of P_{high} and P_{low} extracted from the IFEDF with varying distance between grid G2 and RFEA d_{g}: (a) ion current densities, (b) peak ion energies, (c) full width half maximums and (d) the ratio of ion fluxes $J_{\text{i}}(P_{\text{high}})/J_{\text{i}}(P_{\text{low}})$. Constant parameters: 120 W RF power, 1 Pa He pressure.

The peak energy of the cold ions was between 30 and 35 eV when d_{g} was between 15 and 35 mm. In this range, $d_{\text{g}}/\lambda \gtrsim 1$ and CX collisions are more likely, indicating that this peak energy indeed corresponds to that of cold ions generated by CX collisions. On the other hand, at $d_{\text{g}} = 5$ mm, where $d_{\text{g}}/\lambda \ll 1$, the CX collision probability is lower, as is evident by the negligible flux of P_{low} detected. The peak energy of the cold ions, in this case, was close to 0 eV.

3.1.3. RF power variation. The RF power was varied in the range of 60 to 160 W, keeping the other parameters constant. The IFEDF measurements were obtained at the walls without grid to obtain the sheath properties in the power range used. The $\bar{V}_{\text{s}}$ increased from 66 to 101 V with the increase in the RF power, and the L_{sh} obtained was between 3.7 and 4.3 mm. Hence, the sheath thickness and consequently the plasma–grid interaction is fairly uniform in the experimental power range. Subsequently, grid G2 was installed at $d_{\text{g}} = 35$ mm and the IFEDFs were studied at the walls. The measurements show that increasing RF power influences both the flux and the peak energies of P_{high} and P_{low}, as indicated in figure 8.

As displayed in figure 8(a), the total J_{i} increases with a simultaneous increase in both $J_{\text{i}}(P_{\text{high}})$ and $J_{\text{i}}(P_{\text{low}})$. Increasing the RF power leads to an increase in the degree of ionization and a corresponding rise in the plasma density. This causes a simultaneous increase in the fluxes of both the fast and the cold ions. The ratio of the two ion fluxes, $J_{\text{i}}(P_{\text{high}})/J_{\text{i}}(P_{\text{low}})$, remains a constant at roughly 1.6, as displayed in figure 8(d). As the pressure is 1 Pa, the λ remains constant at roughly 25 mm (figure 5), indicating that the interaction between the fast ion beam and the background neutrals does not change with the increasing RF power, leading to a constant ion flux ratio. A constant flux ratio with increasing ionization power was also observed in [42].

The peak energy of P_{high} increased with the RF power, as observed in figure 8(b). The reason for this is that increasing the RF power increases $\bar{V}_{\text{s}}$ at the grid, causing the rise in the fast ion energy. The peak energy of the P_{low} also increased gradually from 27 to 40 eV. The dispersions of both P_{high} and P_{low} were fairly constant at roughly 8 and 3 eV, respectively, in the power range. It is worth noting that the changing fast ion energy also influences the resonant CX collision cross-section σ_{CX}. However, for incident energies between 80 and 110 eV, σ_{CX} decreases only slightly from 1.6 to 1.5×10^{-19} m^{-2} [44]. This could have an influence on the energy of the newly formed cold ions; however, we cannot say if this is general behavior due to the lack of experimental data.

3.1.4. Grid variation. Finally, a parametric study was carried out with different grids (table 1) to study the impact of changing grid dimensions on the obtained IFEDF at the walls. In this case, the IFEDF properties depend predominantly on the grid-induced effects, as the plasma–grid interaction changes by modifying the grid dimensions.

With the reference parameters, the L_{sh} is 3.8 mm. Hence, with grid G1, the ratio $L_{\text{sh}}/w_{\text{g}} = 2.4$ and $t_{\text{g}}/w_{\text{g}} = 0.14$. This

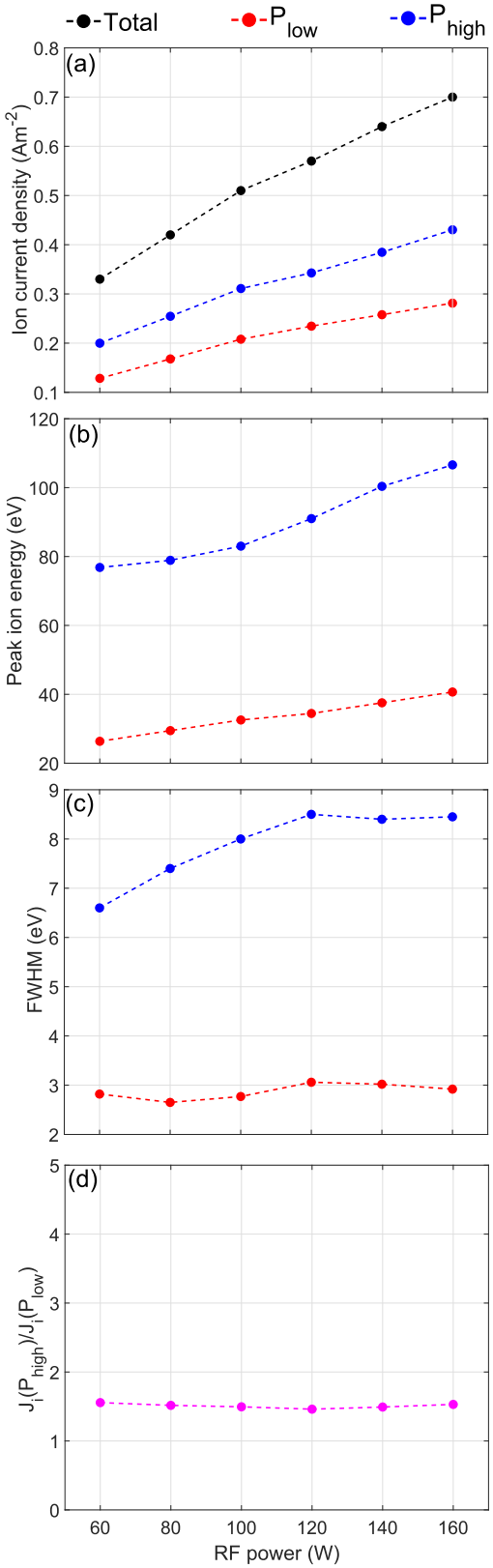

Figure 8. The characteristics of P_{high} and P_{low} extracted from the IFEDF with varying RF power: (a) ion current densities, (b) peak ion energies, (c) full width half maximums and (d) the ratio of ion fluxes $J_i(P_{high})/J_i(P_{low})$. Constant parameters: 1 Pa He pressure, grid G2 at $d_g = 35$ mm.

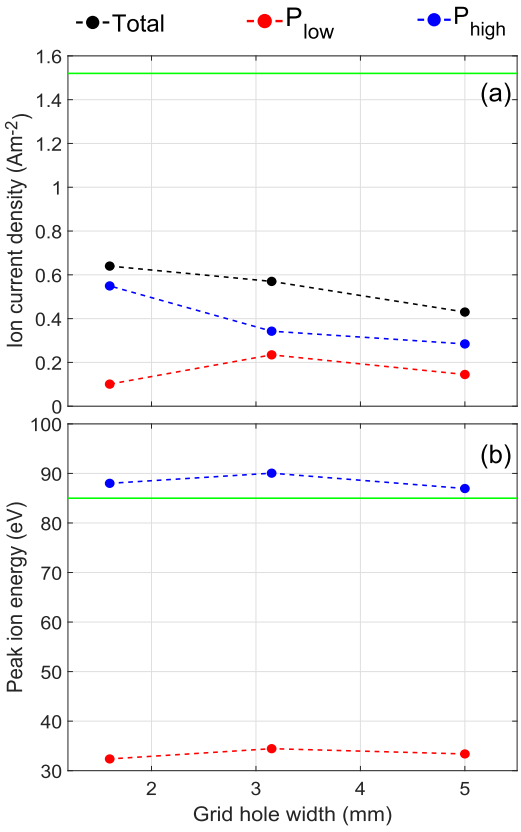

Figure 9. Variation of the ion current density and ion energies of the peaks obtained in the IFEDF across grids of different hole widths. The solid horizontal line in green represents the corresponding value in the IFEDF obtained without grids.

implies that the sheath molding is minimal and the ion beam is rather collimated with negligible grid-induced ion neutralisations. The total ion flux measured in this case is composed of a majority fast ion flux, as displayed in figure 9(a). With grid G2, L_{sh}/w_g decreases to 1.2, pointing to an increasing beam divergence. On the other hand, t_g/w_g remains similar at 0.17, again leading to insignificant neutralisations. The total ion flux remains identical to that obtained with G1; however, with a decreased fast ion and increased slow ion flux. With G3, L_{sh}/w_g further decreases to 0.76, enhancing the beam divergence. Despite an increased sheath molding, the neutralisations can still be neglected as L_{sh}/w_g remains at 0.15. The total ion flux decreases marginally from 0.6 to 0.4 A m^{-2}, while it is composed of both fast and slow ions in a considerable proportion. Consequently, the ratio of the fast and cold ion flux, $J_i(P_{high})/J_i(P_{low})$, is the highest at 5.5 for G1, while it remains low at 1.5 and 2 for G2 and G3, respectively. This suggests that an increasing beam divergence could contribute to an increase in the resonant CX collisions in the collisional volume. However, since the uncertainty in the ion flux measurements can be as high as 20%, the obtained variation in the measurements does not allow us to draw the above-mentioned conclusion. It is worth noting that while the geometric transparency of the grid decreases from G1 to G3, the sheath bending could increase the

ion flux transparency, potentially nullifying the effect. However, with all the grids, the total ion flux at the wall is $\leqslant 40\%$ of the ion flux, reaching the walls without any grids, as observed in figure 9(a). The additional loss in the ion flux besides that coming from the transparency of the grids can be attributed to neutralisations occurring downstream. The beam divergence could also influence the IFEDF measurements in the RFEA [47]; although, such effects would not be significant under our experimental conditions.

Both the fast and the cold ion energies remained nearly constant with all the grids, as displayed in figure 9(b). The fast ion energy was roughly 90 eV, and identical to the ion energy measured in the absence of grids. The cold ion energy, on the other hand, was roughly 35 eV. As both the RF power and the He pressure remain constant, the sheath potential remains unchanged, leading to uniform fast ion energies. In addition, the density of background neutrals remains constant, eliminating any energy damping effects, keeping both fast and cold ion energies constant as observed.

3.2. Influence of grids on wall sputtering and re-deposition on electrodes

As can be inferred from figure 9(a), adding grids between the electrodes and walls reduces the ion current density reaching the wall by over 60%. We can also calculate the approximate wall sputtering rate (R_{ws}) in nm h^{-1} using the following relation,

$$R_{ws} = 3.6 \times 10^6 \times \frac{Y_i J_i}{e} \left(\frac{M}{N_A \rho} \right) \tag{6}$$

where Y_i is the sputtering yield at the mean ion energy, J_i is the ion current density (A m^{-2}), e is the electronic charge, N_A is the Avogadro's number and, M and ρ are the atomic mass (g mol^{-1}) and density (g cm^{-3}) of the wall material, respectively. The Y_i of materials at specific projectile energies can be obtained in the work of Roth *et al* [48]. In the absence of grids, the IFEDF on the walls (with parameters in table 2) comprised of one single peak at 85 eV with a J_i of 1.5 A m^{-2}. This corresponds to an R_{ws} of 18.3 nm h^{-1}. After the addition of grid G2 at $d_g = 35$ mm, the IFEDF with the same parameters comprised two peaks, P_{high} at 90 eV and P_{low} at 34 eV, with a total J_i of 0.6 A m^{-2} (figure 3). Using equation (6), this leads to an R_{ws} of 4.4 nm h^{-1}. This corresponds to a 76% decrease in R_{ws} with the addition of grids. It is worth noting that the 76% decrease calculated for the sputtering rate is merely an estimate to highlight the noticeable decrease in wall sputtering in the gridded reactor. The real decrease can considerably differ from the values calculated via equation (6), given the poor accuracy of Y_i at low ion energies as well as the experimental uncertainty in the measured J_i. A decrease in R_{ws} in the gridded reactor points to a lowering of wall re-deposition on the M1 and M2. To study this experimentally, a long-exposure plasma discharge was conducted in both gridless and gridded plasma reactors.

In our previous study [30], we reported the results of plasma exposure in the gridless reactor. At 120 W RF power and 1 Pa He pressure, the discharge was conducted for 7 h, following which there was considerable wall re-deposition on M1 and M2, where M1 was DC-grounded and M2 was floating. To recall, in a floating state, M2 acquires the floating potential V_f and is sputtered with an ion energy of $e(V_p - V_f)$, which is ∼20 eV in our plasma. Hence, M2 collects all wall deposits with minimal surface sputtering. After the discharge, M2 (figure 10(b)) was coated with a 35 nm thick Cu layer, giving a re-deposition rate R^R_{M2} of 5 nm h^{-1}. Here, R^R_{M2} is also indicative of the rate of re-deposition on M1 (R^R_{M1}), as they are in a geometrically symmetric configuration in the reactor. The DC-grounded powered electrode M1 was homogeneously covered with wall deposits (Cu), as observed in figure 10(a). Since M1 is DC-grounded, both M1 and the Cu walls are sputtered with the same ion energy of eV_p (=90 eV). Hence, the erosion of M1 (with the erosion rate R^E_{M1}) competes with a subsequent re-deposition of the wall material during the discharge. However, $R^R_{M1} > R^E_{M1}$, leading to the growth of a wall deposit layer on its surface over the duration of discharge. The re-deposited layer on the surface was quantified via XPS, which indicated 67 at.% of Cu compared to 33 at.% of Mo.

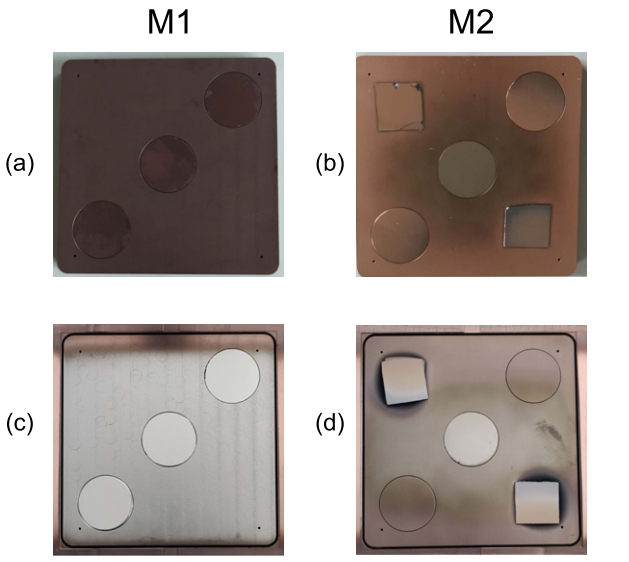

Figure 10. Images of (a) DC-grounded M1 and (b) floating M2 after the experimental discharge without grids Reproduced courtesy of IAEA. Figure from [30]. Copyright (2021) IAEA;
(c) DC-grounded M1 and (d) floating M2 after similar discharge with addition of grids.

In a new experimental campaign, grounded grids were added between M1 and all the surrounding walls to create a 'grid wall' between the electrodes and the Cu walls in the plasma reactor. The distance between the grids and the Cu walls of the plasma reactor was 40 mm. An image of the gridded plasma reactor with confined plasma can be observed in figure S3 of the supplementary information. The plasma parameters were identical to those used in [30], i.e. 120 W RF power, 1 Pa He pressure, and a discharge duration of 7 h. After the experimental discharge, most of M1 was visibly free of wall deposits, as observed in figure 10(c). There was visible deposition concentrated on the top and bottom edge of the electrode where the grids were placed. There was a tiny gap between the grid boundary and the wall, allowing for an edge deposition. The insets of M1 were characterized using

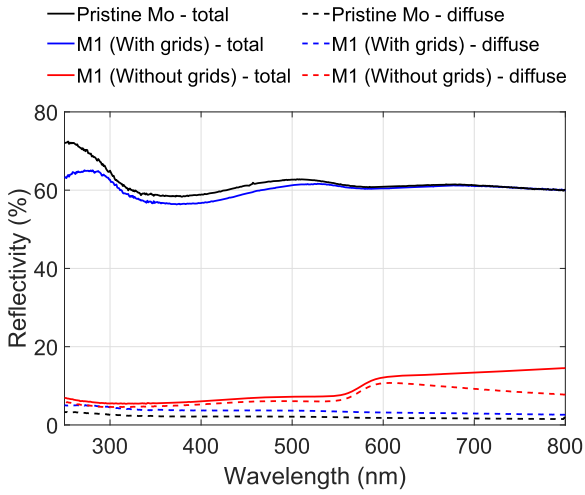

Figure 11. Total and diffuse reflectivities of the central inset of M1 after the experiments in the plasma reactor with and without grids. The total and diffuse reflectivities of a pristine PcMo mirror are also presented for reference.

XPS. The measurement on the central inset displayed a 95 at.% of Mo and 5 at.% Cu, while that on the edge inset led to 90 at.% of Mo, 7 at.% Cu and 2 at.% Fe, indicating a minuscule wall re-deposition on M1. The presence of Fe indicates that the stainless steel grids were sputtered and re-deposited on the edge of M1, although in small amounts. The floating M2 was visibly coated with deposits, as displayed in figure 10(d). XPS measurement on the central inset of M2 showcased 50 at.% of Mo, 28 at.% Cu and 22 at.% Fe, indicating that the Cu and Fe are re-deposited in equivalent amounts. The thickness of the Cu and Fe deposits on the inset were estimated to be ∼15 nm and ∼10 nm, respectively. This gives a Cu and Fe re-deposition rate of 2.1 nm h^{-1} and 1.4 nm h^{-1}, respectively, leading to the net R^{R}_{M2} and hence R^{R}_{M1} of 3.5 nm h^{-1}. While the rate of Cu re-deposition is lowered from 5 to 2.1 nm h^{-1} with the addition of grids, the sputtering of grids led to an additional re-deposition rate of 1.4 nm h^{-1}. Despite the non-negligible R^{R}_{M1}, M1 was free of wall deposits, thus showing that it was in a state of net erosion, i.e. $R^{E}_{M1} > R^{R}_{M1}$.

The reflectivity of the central inset of M1 from the gridless and the gridded plasma reactor was measured in the wavelength range of 250 to 800 nm. Since the reflectivities are more sensitive at lower wavelengths, we shall only discuss the values at $\lambda = 250$ nm. Due to the Cu deposition in the gridless plasma reactor, the total reflectivity of the inset was extremely low at 7% and comparable to the diffuse reflectivity, as observed in figure 11. As a result, the specular reflectivity was negligible at roughly 1%. With the gridded plasma reactor, however, the total reflectivity of the inset after the experiment was high at 64%. A pristine poly-crystalline Mo (PcMo) mirror, unrelated to this experiment, was used as a reference to compare with the reflectivity of the inset. The reflectivity of the pristine PcMo mirror can be obtained in [49]. As observed in figure 11, the total reflectivity of the inset was at the pristine PcMo level (72%). The diffuse reflectivity of the inset was also low at 5%. The specular reflectivity of the inset was 59% compared to 68% of a pristine PcMo mirror.

The results clearly indicate that confining the plasma with grounded grids in a plasma reactor can significantly reduce the sputtering of the reactor walls and its re-deposition on the powered electrode during the RF discharges in the presence of a $\lambda/4$ filter. Furthermore, even though the grids are sputtered, the DC-grounded electrode tends to remain in an erosion-dominated regime, keeping it relatively clean of wall and grid deposits. In addition to a clean surface, the reflective properties of the electrode are preserved after the discharge to near-pristine levels. The use of grounded grids before the walls hence provides a promising mitigation strategy for RF discharge cleaning of FMs while maintaining their optical properties, in the presence of a $\lambda/4$ filter in ITER diagnostics.

4. Conclusion and outlook

In this study, we experimentally investigated the ion flux–energy distributions across grounded grids in a CCRF plasma reactor. The experiments were conducted by igniting He discharges in the reactor via a DC-grounded powered electrode. Grids of different dimensions were placed between the powered electrode and the reactor wall to confine the plasma. The flux–energy distributions of the ion beam departing the grids and reaching the reactor walls were studied using an RFEA with varying plasma parameters.

The IFEDFs obtained at the walls were double-peaked, indicating the presence of two ion groups: (i) fast ions arriving from the plasma forming the high energy peak P_{high}, and (ii) cold ions generated downstream upon CX collisions of the fast ions with background neutrals, forming the low energy peak P_{low}. The flux as well as peak energies of the two ion groups depended considerably on the process parameters, as follows:

- Increasing the He pressure led to a change in both the fast and cold ion energies. However, the increased pressure contributed to an increased cold ion formation and the fast ion flux decreased exponentially.
- Increasing the distance between the grid and the wall d_g kept the fast and cold ion energies nearly constant as long as $d_g \gtrsim \lambda$, with λ being the CX mean free path. However, with increased CX collisions, the fast ion flux transferred to the cold ion flux, and hence it attenuated exponentially.
- Increasing the RF power or the ionizing potential led to an increase in the fast and cold ion energies while keeping their flux ratio nearly constant.
- Increasing the grid hole size in the range of the sheath thickness kept both the fast and cold ion energies uniform, while the cold ion flux appeared to increase, albeit in a narrow range.

The results indicate that the addition of grids between DC-grounded electrodes and reactor walls, such that the plasma

is confined, can reduce the ion flux at the walls by over 60% with a significant lowering of the wall sputtering rate. This was verified in a long plasma exposure in a gridded plasma reactor, wherein the powered electrode was sputtered with a high flux of fast ions from plasma, while the walls were sputtered with a relatively low flux as well as a mix of fast and cold ions. The resulting electrode surface was free of wall deposits, although with an edge deposition. The grids were however sputtered in this case and deposited on the electrode, although in negligible amounts. The specular reflectivity of the electrode surface after the discharge was preserved to pristine levels, indicating no surface deterioration. In contrast, a similar discharge without grids resulted in the coating of electrode surface with 35 nm of wall deposits and a significant drop in the surface reflectivity [30].

The results are of great importance in ion extraction sources as well as ensuing ion–surface interactions. By varying the system parameters a greater degree of control can be achieved on both the flux of the incoming ions as well as their energy on material surfaces. This also calls for further work in the study of plasma–grid interactions, to enhance the knowledge of the ion loss mechanisms as well as the production of slow ions via CX collisions. The dependence of slow ion production on ion beam divergence as well as grid-induced ion neutralisations via grids with wider and thicker holes is also an interesting topic for further study.

The results are particularly promising for the application of plasma cleaning of DC-grounded FMs in ITER diagnostic systems. As the FMs experience a threat of wall deposition during plasma cleaning with a $\lambda/4$ filter, installing grids between the FMs and adjacent walls can serve as an excellent mitigation strategy by limiting the plasma-wall interaction and its sputtering. The ion flux as well as the energy load on the walls in this case can be controlled by varying the process and system parameters, as discussed above. In ITER, the plasma cleaning is also projected to be conducted in the presence of a high magnetic field of 3 to 5 T. The B field can change the sheath properties and the plasma-grid interaction. Hence, the influence of the B field on plasma cleaning of FMs in gridded reactors as well as sputtering of wall surfaces is a highly relevant topic for further study, currently under investigation by the authors of this work, and whose results will be discussed in a future publication.

Acknowledgments

This work was supported by the ITER Organization under I/O Contract IO/18/CT/4300001749. This work has also been carried out within the framework of the EUROfusion Consortium and has received funding from the Euratom research and training programme 2014–2018 and 2019–2020 under grant Agreement No. 633053. The views and opinions expressed herein do not necessarily reflect those of the ITER Organization or European Commission. The Swiss Federal Office of Energy, Swiss Nanoscience Institute, Swiss National Science Foundation and the Federal Office for Education and Science are acknowledged for their financial support.

Data availability statement

The data that support the findings of this study are available upon reasonable request from the authors.

ORCID iDs

Kunal Soni https://orcid.org/0000-0002-8786-7365
Rodrigo Antunes https://orcid.org/0000-0001-9993-7247
Roland Steiner https://orcid.org/0000-0002-4350-4132
Lucas Moser https://orcid.org/0000-0003-1766-9942
Laurent Marot https://orcid.org/0000-0002-1529-9362
Ernst Meyer https://orcid.org/0000-0001-6385-3412

References

[1] Lieberman M A and Lichtenberg A J 2005 *Principles of Plasma Discharges and Materials Processing* (New York: Wiley)
[2] Chabert P and Braithwaite N 2011 *Physics of Radio-Frequency Plasmas* (Cambridge: Cambridge University Press)
[3] Makabe T and Petrovic Z L 2006 *Plasma Electronics: Applications in Microelectronic Device Fabrication* (Boca Raton, FL: CRC Press)
[4] Schulze J and Mussenbrock T 2016 *Plasma Sources Sci. Technol.* **25** 020401
[5] Wild C and Koidl P 1989 *Appl. Phys. Lett.* **54** 505–7
[6] Wild C and Koidl P 1991 *J. Appl. Phys.* **69** 2909–22
[7] Donkó Z, Schulze J, Czarnetzki U, Derzsi A, Hartmann P, Korolov I and Schüngel E 2012 *Plasma Phys. Control. Fusion* **54** 124003
[8] Rossnagel S M, Cuomo J J and Westwood W D 1990 *Handbook of Plasma Processing Technology: Fundamentals, Etching, Deposition, and Surface Interactions* 1 edn (Norwich, NY: William Andrew)
[9] Economou D J 2008 *J. Phys. D: Appl. Phys.* **41** 024001
[10] Kaufman H R, Cuomo J J and Harper J M E 1982 *J. Vac. Sci. Technol.* **21** 725–36
[11] Ensinger W 1992 *Rev. Sci. Instrum.* **63** 5217–33
[12] Holste K *et al* 2020 *Rev. Sci. Instrum.* **91** 061101
[13] Kim C-K and Economou D J 2002 *J. Appl. Phys.* **91** 2594–603
[14] Panda S, Economou D J and Chen L 2001 *J. Vac. Sci. Technol.* A **19** 398–404
[15] Toyoda N and Matsui S 2014 Ion Beam Deposition: Recent Developments *Comprehensive Materials Processing* vol 4 (Amsterdam: Elsevier) pp 187–200
[16] Leipold F *et al* 2016 *Rev. Sci. Instrum.* **87** 11D439
[17] Litnovsky A *et al* 2019 *Nucl. Fusion* **59** 066029
[18] Soni K, Moser L, Steiner R, Mathys D, Le Guern F, Piqueras J, Marot L and Meyer E 2019 *Nucl. Mater. Energy* **21** 100702
[19] Soni K, Moser L, Porosnicu C, Antunes R, Arredondo R, Dinca P, Steiner R, Marot L and Meyer E 2022 *J. Nucl. Mater.* **564** 153671
[20] Dmitriev A M *et al* 2017 *Phys. Scr.* **T170** 014072
[21] Ushakov A *et al* 2018 *Fusion Eng. Des.* **136** 431–7
[22] Shigin P *et al* 2021 *Fusion Eng. Des.* **164** 112162
[23] Campbell D J *et al* 2019 *J. Fusion Energy* **38** 11–71
[24] Soni K *et al* 2021 *Plasma Phys. Control. Fusion* **63** 045005
[25] Collins G A and Tendys J 1994 *J. Vac. Sci. Technol.* B **12** 875–9
[26] Köhler K, Coburn J W, Horne D E, Kay E and Keller J H 1985 *J. Appl. Phys.* **57** 59–66
[27] Köhler K, Horne D E and Coburn J W 1985 *J. Appl. Phys.* **58** 3350–5

[28] Aanesland A, Charles C, Boswell R W and Lieberman M A 2005 *Phys. Plasmas* **12** 103505
[29] Faudot E, Ledig J, Moritz J, Heuraux S, Lemoine N and Devaux S 2019 *Phys. Plasmas* **26** 083503
[30] Soni K, Steiner R, Antunes R, Moser L, Shigin P, Reichle R, Marot L and Meyer E 2021 *Nucl. Fusion* **61** 126017
[31] Marot L *et al* 2021 *Fusion Eng. Des.* **163** 112140
[32] Schulze J, Schüngel E, Donkó Z and Czarnetzki U 2011 *Plasma Sources Sci. Technol.* **20** 015017
[33] Gahan D, Daniels S, Hayden C, Sullivan D O and Hopkins M B 2012 *Plasma Sources Sci. Technol.* **21** 015002
[34] Eren B, Marot L, Langer M, Steiner R, Wisse M, Mathys D and Meyer E 2011 *Nucl. Fusion* **51** 103025
[35] Pouchou J and Pichoir F 1993 *Scanning Microsc.* **7** 12 https://digitalcommons.usu.edu/microscopy/vol1993/iss7/12
[36] Rickerby D G and Thiot J-F 1994 *Mikrochim. Acta* **114–115** 421–9
[37] Galbert F 2007 *Microsc. Microanal.* **13** 96–7
[38] Moser L 2017 Plasma cleaning of diagnostic first mirrors for the nuclear fusion machine ITER *PhD Thesis* University of Basel
[39] Child C D 1911 *Phys. Rev. Ser.* I **32** 492
[40] Langmuir I 1913 *Phys. Rev.* **2** 450
[41] Harhausen J, Brinkmann R P, Foest R, Hannemann M, Ohl A and Schröder B 2012 *Plasma Sources Sci. Technol.* **21** 035012
[42] Zian W, Jinxiu M, Yuanrui L, Yan S and Zhengqi J 2016 *Plasma Sci. Technol.* **18** 1076
[43] Sakabe S and Izawa Y 1992 *Phys. Rev.* A **45** 2086
[44] Sakabe S and Izawa Y 1991 *At. Data Nucl. Data Tables* **49** 257–314
[45] Bromley S J, Fox D C, Sosolik C E, Harriss J E and Marler J P 2018 *Rev. Sci. Instrum.* **89** 073107
[46] Lindsay B and Stebbings R 2005 *J. Geophys. Res.: Space Phys.* **110** A12213
[47] Edelberg E A, Perry A, Benjamin N and Aydil E S 1999 *J. Vac. Sci. Technol.* A **17** 506–16
[48] Eckstein W, Garcia-Rosales C, Roth J and Ottenberger W 1993 Sputtering data *Report Ipp 9/82*
[49] Moser L, Steiner R, Leipold F, Reichle R, Marot L and Meyer E 2015 *J. Nucl. Mater.* **463** 940–3